Atmospheric
Chemistry
and Physics
Discussions

Aerosol Effects on Electrification and Lightning Discharges in a Multicell Thunderstorm Simulated by the WRF-ELEC Model

Mengyu Sun[1,5], Dongxia Liu[1], Xiushu Qie[1], Edward R. Mansell[2], Yoav Yair[3], Alexandre O. Fierro[2,4], Shanfeng Yuan[1], Zhixiong Chen[1,5], Dongfang Wang[1]

5

[1] Key Laboratory of Middle Atmosphere and Global Environment Observation, Institute of Atmospheric Physics, Chinese Academy of Sciences, Beijing, China

[2] NOAA/National Severe Storms Laboratory, Norman, Oklahoma, USA

[3] Interdisciplinary Center (IDC) Herzliya, School of Sustainability, Herzliya, Israel

10 [4] Cooperative Institute for Mesoscale Meteorological Studies, University of Oklahoma, Norman, Oklahoma, USA

[5] College of Earth and Planetary Sciences, University of Chinese Academy of Sciences, Beijing, China

15 *Correspondence to*: Dongxia Liu (liudx@mail.iap.ac.cn)

Abstract

To investigate the effects of aerosol on lightning activity, the Weather Research and Forecasting (WRF) Model with a two-moment bulk microphysical scheme and bulk
20 lightning model was employed to simulate a multicell thunderstorm that occurred in the metropolitan Beijing area. The results suggest that under polluted condition lightning activity is significantly enhanced during the developing and mature stages, while it is being delayed at the initial stage. Electrification and lightning discharges within the thunderstorm show distinguish characteristics by different aerosol conditions through
25 microphysical processes. Elevated aerosol loading increases the cloud droplets numbers, the latent heat release, updraft and ice-phase particle number concentrations. More

negative charges in the upper level are carried by ice particles and enhance the electrification process. A larger effective radius of graupel particles further increases non-inductive charging due to more effective collisions. The first lightning discharge

30   was delayed at the beginning of polluted thunderstorm, coincident with the delayed occurrence of graupel and ice particles, which are responsible for charge generation through the non-inductive mechanism. In the continental case where aerosol concentrations are low, less latent heat releases in the upper parts of the cloud and as a consequence, the updraft speed is weaker leading to smaller concentrations of ice

35   particles, lower charging rates and less lightning discharges.

1 Introduction

Lightning activity is related to two important factors: dynamic-thermodynamic and microphysical characteristics (e.g. Williams et al., 2005; Guo et al., 2016; Wang et

40   al., 2018; Zhao et al., 2020). Since the dynamic-thermodynamic processes affect the development of thunderstorm significantly, lightning activity is influenced by various dynamic-thermodynamic variables: temperature (Price, 1993), relative humidity in the lower and middle troposphere (Xiong et al., 2006; Fan et al., 2007), and convective available potential energy (Qie et al., 2004; Stolz et al., 2015), and many others.

45   The impacts of aerosol on the development of thunderstorm especially in metropolitan areas have been researched extensively. Observational studies indicated that the enhancement of lightning activity was related to increased cloud condensation nuclei (CCN) concentration (e.g., Westcott, 1995; Orville et al., 2001; Kar et al., 2009; Wang et al., 2011; Chaudhuri and Middey, 2013; Thornton et al., 2017; Yair, 2018). Kar

50   et al. (2009) found a positive correlation between PM10 and SO_2 concentration and lightning flash densities around major cities in South Korea. A positive relationship between levels of particle pollution and lightning flash counts was also indicated by Chaudhuri and Middey (2013).

Furthermore, a variety of numerical simulations (e.g., Mitzeva et al., 2006)

55   demonstrated the effects of aerosol on enhancing lightning activity. Using the Weather

Research and Forecasting (WRF) Model with explicit spectral bin microphysics, Khain et al. (2010) found elevated aerosol increased the number of cloud droplets and the release of latent heat by acting as CCN. Therefore, more liquid water was lifted to mixed-phase region by strong updrafts, with more ice-phase particles produced which

60 can affect charge separation and lightning formation (Takahashi, 1978; Saunders and Peck, 1998; Takahashi et al., 1983; Mansell et al., 2005; Yair, 2008). Mansell and Ziegler (2013) suggested that greater CCN concentration led to greater lightning activity up to a point by testing a wide range of CCN concentration in a 3D model with two-moment bulk microphysics and stochastic branched discharge parameterization

65 (Mansell et al., 2002). They also noted that average graupel density stayed high at lower CCN, but dropped at higher CCN because smaller droplets caused lower rime density. Zhao et al. (2015) showed that enhancing aerosol concentration resulted in an enhancement of electrification processes, due to the increasing growth rate of snow and graupel particles. However, Tan et al. (2017) simulated a thunderstorm in Changchun

70 city with a 3D cumulus model coupled with aerosol module, electrification and lightning discharge, showing that the ice crystal and graupel number increased while the graupel mixing ratio decreased as the aerosol concentration increased.

The microphysical processes under different CCN concentration, especially the initiation and growth of ice-phase particles varied from different simulation studies.

75 There are few studies that discussed the aerosol effects on thunderstorm with explicit electrification and discharge parameterization in the model simultaneously (e.g., Mitzeva et al., 2006; Mansell and Ziegler, 2013; Zhao et al., 2015). Simulation by Tan et al. (2017) showed that elevated aerosol loading delayed the first discharge but rarely analyzing the microphysical reasons. The detailed effects of aerosol on the delay of

80 discharging need further study.

By analyzing lightning data from the Beijing Lightning Network (BLNET) and PM2.5 data, Sun et al. (2020) found a positive relationship between flash counts and PM2.5 concentration prior to the occurrence of thunderstorm. As a mega city, Beijing has higher aerosol concentration resulting from anthropogenic air pollution. Still, the

85 effects of aerosol on both electrification and discharges have been rarely discussed in

this area by numerical simulation. Therefore, in this paper we present sensitivity studies on how the different CCN concentration influence the characteristic of thundercloud over the metropolitan Beijing area using the WRF-ELEC (Fierro et al., 2013). We conducted sensitivity studies to evaluate the response of the microphysical properties,

90 as well as electrification and lightning processes to aerosol characteristics. This paper is organized as follows: section 2 describes the data and methodology used in the study, section 3 introduces the design of simulations, section 4 presents the results, and section 5 discusses and summarizes the study.

95 **2 Data sources**

2.1 Lightning data

Total flash numbers were obtained from the Beijing Lightning Network (BLNET), which consists of 16 stations covering East-West 110 km and North-South 120 km areas since 2015. The BLNET provides 3D-location results of flashes, including both intra-

100 cloud (IC) and cloud-to-ground (CG) lightning (Wang et al., 2016). The average detection efficiency of the BLNET is 93.2% for the total flashes (Srivastava et al., 2017). In this study, the 3D-location lightning radiation pulses were grouped in flashes based on the criteria of 400 ms and 15 km. This grouping criteria was modified from the algorithm in Srivastava et al. (2017). In section 3, the lightning frequency from BLNET

105 was calculated in every 6 min intervals, corresponding to the time span of Doppler radar scanning.

2.2 Radar data

In addition, the radar reflectivity data was obtained from an S-band Doppler radar (Chinese CINRAD/SA) near Beijing urban area (39.81 °N, 116.47 °E), and were updated

110 every 6 min. The vertical levels vary from 500 m to 20 km and were processed into composite radar reflectivity with a horizontal resolution (0.01 °×0.01 °).

Atmospheric
Chemistry
and Physics
Discussions
Open Access
EGU

2.3 Synoptic background

A mesoscale convective system over the Beijing area influenced by a strong Mongolia cold vortex on 11 Aug 2017 was simulated in this study. Based on the weather

115   map at 00:00 UTC (figure not shown), there was a prevailing westward airflow in the south of the cold vortex, which brought dry cold air in middle layer. At low-level of 850 hPa, the southwesterly jet transported warm and humid air mass, forming an unstable condition together with cold air mass above. The sounding profile over Beijing (39.9 °N, 116.2 °E) exhibited an unstable thermodynamic condition for thunderstorm

120   initialization, as shown in Fig. 1, with a surface-based convective available potential energy (CAPE) of 3937 J kg^{-1} at 12:00 UTC. The special terrain condition with mountain in the northwest and ocean in the southeast (Qie et al., 2020), as well as heat island effect and elevated aerosol loading in the urban region, likely enhanced the convection and were responsible for the occurrence of heavy rainfall and intensive

125   lightning activity in the Beijing area. According to the surface-based automatic weather observation network in Beijing, the average rainfall in the urban area and the eastern region was 10-30 mm, with locally exceeding 100 mm. The maximum total lightning frequency even exceeded 1600 flashes (6 min)$^{-1}$ at the mature stage.

130   **3. Model overview**

The WRF (version 3.9.1) model coupled with bulk lightning model (BLM, Fierro et al., 2013) and a two-moment bulk microphysics scheme (Mansell et al., 2010; Mansell and Ziegler, 2013) was used to simulate the multicell thunderstorm that occurred on 11 August 2017 in the Beijing metropolitan area.

135   The two-moment bulk microphysics scheme predicts both mass mixing ratio and number concentration for a range of hydrometeor species (droplets, rain, ice crystals, snow, graupel, and hail). The graupel growth process contains the following processes: collection of ice crystals by graupel, collection of snow particles by graupel, deposition of vapor to graupel, collection of supercooled water (cloud droplets and/or raindrops)

Atmospheric
Chemistry
and Physics
Discussions

140   by graupel, and conversions between hydrometeors. The CCN concentration is
      predicted as a bulk activation spectrum and initially mixed well vertically. The initiation
      of cloud droplets (both for cloud base and in-cloud) uses an expression based on
      Twomey (1959).

      Explicit charging physics includes both non-inductive charging (Saunders and
145   Peck, 1998) and inductive or polarization charging (Ziegler et al., 1991). Non-inductive
      charge separation resulting from rebounding collisions between graupel-hail and snow-
      cloud ice are all parameterized (Mansell et al., 2005). Numerical experiments (Mansell
      et al., 2010) found that total inductive charging is about an order of magnitude weaker
      than non-inductive charging, but can be important for lower charge regions. Only
150   collisions between cloud droplets and ice-phase particles (graupel, ice, hail) are
      considered for inductive electrification. The discharge model parameterization from
      Ziegler and MacGorman (1994) is used within a cylindrical region (Fierro et al. 2013),
      whereby a flash would be initiated when the electric field exceeds a breakdown
      threshold at a model grid point (from here on, we shall use the term 'grids' for short).

155   An estimate of flash origin density (FOD) rate (over a time period $T = t_2 - t_1$) is
      computed following Eq. (1) of Fierro et al. (2013):

$$FOD(T) = \frac{G}{C} \int_{t_1}^{t_2} B(t)dt, \tag{1}$$

      where G is the horizontal grid cell area, C the cylinder cross sectional area and the
      integral represents the sum of all discharge locations $[B(t)]$ counts for all the time steps
160   within the time period T. Further, lightning discharge events (LDE) are given by Eq. (2)
      of Fierro et al. (2013). Thus, the predicted lightning frequency over the Beijing area in
      section 3 is the LDE calculated in 6 min intervals:

$$LDE(T) = \sum FOD(T). \tag{2}$$

3.1 Design of the simulations

The nested model configuration for the simulations are shown in Table 1. The $1°×1°$NCEP GFS (Global Forecast System) data is used to establish the initial and boundary conditions.

To survey the aerosol effects on the structure of thunderstorm and lightning activity, two sensitivity experiments are performed with different CCN concentration: a polluted case (P-case) and a continental case (C-case). The average value of the observed aerosol concentration before the thunderstorm initiation is much higher in the Beijing area (Sun et al., 2020), therefore, the CCN concentration is selected as the P-case which is consistent with observation. The initial value for the P-case is set as a number mixing ratio relative to sea level air density ρ_0: $2000/\rho_0$ kg^{-1}, where ρ_0=1.225, and the local number concentration is $2000×(\rho_{air}/\rho_0)$ cm^{-3}. And the initial number concentration for the C-case is set at $1200×(\rho_{air}/\rho_0)$ cm^{-3}, consistent with continental conditions (e.g. Hobbs and Rangno, 1985; Mansell et al., 2005; Mansell, personal communication, 2019). The relatively high prescribed CCN concentration guaranteed small droplet diameters and effectively delayed the warm rain process in the model (Mansell and Ziegler, 2013).

4 Results

4.1 Radar reflectivity and lightning flashes of multicell

Figure 2 shows the observed and simulated radar reflectivity at different periods for both cases, with the formation of thunderstorms in the simulation earlier than the observation about 1.5 h. For this reason, we display the simulation and observation with ~90 minutes time difference. It is clear that both simulated times exhibit an overall good agreement with the evolution and morphology of the radar echo, especially evidenced by the northeast-southwest orientation of the radar echo at 11:54 UTC in the simulated (13:24 UTC in the observation) reflectivity fields. Note that the modeled reflectivity

Atmospheric
Chemistry
and Physics
Discussions

Open Access
EGU

differs from the observation in the northwestern area (116.4 °E-116.0 °E, Fig. 2a, 2c and 2e), and so the impacts of aerosol on lightning activity will only be evaluated in the southeastern Beijing area (116.0 °E-117.5 °E).

195 The temporal variation of total flashes from BLNET is shown in Figure 3a, including both intra-cloud (IC) and cloud-to-ground (CG) lightning. The lightning frequency gradually increased during 11:00-12:00 UTC and raised significantly after 12:00 UTC, as well as reached the peak value at 12:30 UTC, and then decreased gradually. According to the evolution of radar reflectivity and lightning activity, the

200 thunderstorm was divided into four periods: the beginning stage (before 11:00 UTC), the developing stage (11:00-12:30 UTC), the mature stage (12:30-13:30 UTC) and the dissipating stage (after 13:30 UTC) of the thunderstorm. The temporal evolution of predicted lightning frequency over Beijing area under the polluted and continental cases are shown in Fig. 3b, both of them start earlier than observation about 1.5 h. The

205 variation of flashes in the P-case is better consistent with the observation. In contrast, the occurrence of the first lightning for the continental case is earlier than both the observation and the polluted case.

 Figure 4 displays the number of initiations over the Beijing area for the C-case and P-case during different periods. To examine the details of lightning response to aerosol,

210 the intensity of lightning activity can be categorized into four levels by the lightning grids in each time step: light (50-100 grids), moderate (100-200 grids), heavy (200-300 grids) and extreme (>300 grids). Then the number of points (grid columns) in each category is counted hourly as the 'number of initiations'. A comparison of the different intensity categories reveals that the simulated lightning activities increase during 10:30-

215 11:30 UTC (Fig. 4c) under high aerosol loading, corresponding to the developing and mature stages of the thunderstorm. During 09:30-10:30 UTC, while different categories of lightning are enhanced for both P- and C-case (Fig. 4b), it is noted that the maximum lightning initiation occurs in the extreme level for the P-case. There is no lightning initiation for the P-case at the beginning of the thunderstorm (08:30-09:30 UTC, Fig.

220 4a), however, all categories of lightning are initiated in the C-case, indicating that the first discharging is delayed under polluted condition. This phenomenon is accordant

Atmospheric
Chemistry
and Physics
Discussions

Open Access

EGU

with previous simulation by Tan et al. (2017), which suggested that the first discharge time of the polluted thundercloud was delayed.

Hence, the results indicate that while elevated aerosol loading enhances lightning activities in the developing and mature stages of thunderstorm, the time of the first discharge is delayed. In the following contents we will offer a possible explanation for this effect.

4.2 Microphysical properties of multicell

To investigate the effects of aerosol on lightning activities, we first analyze the simulated microphysical properties in both the continental and polluted sensitivity studies. Figure 5a-5h show the temporal variations of mass mixing ratio and number concentration for different categories of hydrometeors with the vertical profiles, herein, their mass mixing ratios are averaged horizontally. Figure 5i-5j show the time-height plots of maximum radar reflectivity and vertical velocities. The time-height plots of cloud droplets (Fig. 5a, 5b), raindrops (Fig. 5c, 5d), graupel (Fig. 5e, 5f) and maximum radar reflectivity (Fig. 5i, 5j) in both cases show that three maxima occur at about 09:00 UTC, 10:00 UTC, and 11:30 UTC, corresponding to different stages of the thunderstorm.

It can be seen that elevated aerosol loading results in increasing cloud droplets concentrations especially at the early development stages (Fig. 5b). In previous studies, more aerosols could be activated into cloud droplets and more water vapor condenses onto these droplets, leading to large cloud water content and small droplet size under polluted condition (Lynn et al., 2007; Wang et al., 2011; Zhao et al., 2015; Jiang et al., 2017). However, in this study, more cloud droplets in the P-case probably not result from condensation but come from less conversion to raindrops. This is because the CCN concentration in the C-case is already high and the supersaturations are probably close to zero after condensation of water vapor. The additional CCN in the P-case could not lead to further condensation, which is also evidenced by the similar vertical profiles of latent heating in both cases at 2-10 km, as shown in Fig. 10. Therefore, the more cloud

250   droplets could not simply be explained by more condensation. The domain-averaged

effective radius for cloud droplets is displayed in Fig. 6a, with smaller effective radii

under polluted condition. The maximum effective radii of cloud droplets are 9.62 μm,

8.98 μm and 9.50 μm in different stages for the continental case, and 7.80 μm, 7.72 μm

and 7.42 μm for the polluted case, respectively. Smaller droplets size in the P-case

255   suppresses collection/coalescence processes. The less conversion to raindrops in turn

keeps more mass in droplets, which could be the main reason for more cloud water in

the P-case at early stages.

Consequently, the warm rain process is delayed and the rainwater mass mixing

ratio is less in the polluted case compared with the continental one (Fig. 5d). Cloud

260   droplets, which are too small to be converted into raindrops, could be transported above

freezing level. Previous observations and simulations found that the content of ice

crystals could be greater under polluted condition, resulting from more condensation

latent heat and strengthened updrafts (Khain et al., 2008; Koren et al., 2010). In this

study, the cloud droplets condensation and corresponding latent heat in both cases are

265   approximately the same. More mass loading of droplets in the P-case, however, might

lead to weak updrafts at lower level (Fig. 5j). The cloud ice content is still higher in the

P-case, probably owing to higher droplets content and droplets freezing. As shown in

Fig. 5h, the mass mixing ratio of ice crystals gradually increased with the development

of thunderstorm, with domain-average of 12.74×10^{-2} g kg^{-1} for the polluted case and

270   11.39×10^{-2} g kg^{-1} for the continental case at the mature stage (around 11:30 UTC).

In contrast, the mass mixing ratio of graupel was relatively less in the P-case (Fig.

5f). Less graupel content under polluted condition is rather surprising, since previous

simulation studies (Wang et al., 2011; Zhao et al., 2015) found that there could be more

graupel at the mature stage of thunderstorm, by virtue of enhanced convection and more

275   cloud droplets lifted to the mixed-phase region. These could happen if starting from a

much lower CCN concentration (< 400 cm^{-3}), in this study, with higher CCN

concentration (> 1000 cm^{-3}), the reduced raindrops freezing (Fig. 5d) probably explain

the lower density of graupel. Lower fall speed of the lower density graupel further

results in less riming. Other simulation also found a decrease of graupel mixing ratio

10

280　under polluted condition, and partly attributed the decrease to the melting of graupel

particles (Tan et al., 2017). However, the maximum mixing ratio of graupel in the

polluted case is much larger compared to the continental one especially at the mature

stage. The mean mixing ratio at the mature and dissipating stages were 17.23×10^{-3} g kg^{-1},

41.70×10^{-3} g kg^{-1} for the P-case, and 8.31×10^{-3} g kg^{-1} and 41.53×10^{-3} g kg^{-1} for the

285　C-case, respectively. Such a phenomenon partly explains the appearance of graupel of

larger effective radius in the P-case (Fig. 6c). The effective radii of graupel reached

0.98 mm and 0.92 mm for the P-case, corresponding to 0.71 mm and 0.61 mm in

different stages for the C-case. Compared to the small difference in effective radii of

ice crystals between the polluted and continental cases (Fig. 6d), the radius of graupel

290　is much larger in the P-case, which likely resulted in a larger collision efficiency

between graupel particles and other ice-phase particles, enhancing non-inductive

charging.

　　　　Increasing aerosol loading affects the development of microphysical processes,

especially the ice-phase processes with more ice crystals and larger graupel size. Both

295　of them would inevitably affect lightning activity by affecting the rate and magnitude

of electrification.

4.3 The relationship between hydrometeors and electrification

　　　　To analyze the relationship between hydrometeors and electrification, vertical

cross sections is shown in Figure 7a and 8a, which display the total charge distribution

300　at the mature stage of the thunderstorm in the polluted (11:54 UTC) and continental

(11:24 UTC) cases. In the polluted case, a negative charge region appears in the upper

level (> 13 km), with the positive and negative charge centers located in the middle and

lower level, respectively. The dipolar charge structure with positive charge in the upper

level and negative charge in the lower level simulated in the C-case cannot be classified

305　as simple dipoles or tripoles (Williams et al., 1989) and, is more consistent with

previous observations (Thomas et al., 2001) and simulations (Fierro et al., 2013; Zhao

et al., 2015). As for the total net space charge density, the maximum of positive charge

density at the mature stage in the P-case is up to +1 nC m^{-3}, which is much higher than that in the C-case (< +0.5 nC m^{-3}).

310   We attempt to explain the origins of the charge distribution by examining the polarity and amount of charge carried by different hydrometeor species (namely by ice, graupel, snow and hail particles). The negative charge region in the upper level (12-15 km) results from collision of graupel with smaller ice crystals and snow particles (Fig. 7d), with the 30 dBZ echo tops reaching 13 km. The simulated vertical distribution of

315   net charge in the C-case is caused by ice and snow particles charged positively at 8-13 km and graupel particles charged negatively at 4-10 km, respectively (Fig. 8b and 8d). However, less ice-phase particles appear in upper level in the C-case, corresponding to a relatively weaker negative charge center. Figure 7c and 8c show the cross sections of the simulated radar reflectivity and vertical velocity at 11:54 UTC (11:24 UTC) under

320   different aerosol conditions. It is evident that both updraft and downdraft in the polluted case at higher level are greater than that in the continental one, resulting from more freezing of droplets to ice-phase particles, and as a consequence, the total charge density is significantly larger above 12 km.

        Figure 7d shows that graupel and hail particles charged negatively at 4-8 km, as a

325   result of the non-inductive charging within region of relatively weak updrafts (< 5 m s^{-1}) in the P-case (Saunders and Peck, 1998). With large liquid water content (LWC) in the polluted case, graupel, ice and hail were charged positively, forming an intense positive charge center at 9km (< -20 ℃), as shown in Fig. 7a. The simulations show that non-inductive charging mechanism plays a main role at the mature stage, the rate

330   of which is one order of magnitude larger than inductive charging (Fig. 9). As described in section 4.2, more ice particles and graupel with larger radii appear at this stage in the P-case, evidenced by the larger simulated radar reflectivity (Fig.7c), and the ensuing collision rates led to significantly stronger non-inductive charging at 6-10 km (Fig. 9b). In consequence, it is obvious from Fig. 7a and 8a that the charge density for the P-case

335   is much higher than the C-case, indicating that aerosol plays an important role in affecting the accumulated charge density through microphysical and electrical processes.

Atmospheric
Chemistry
and Physics
Discussions

Open Access

EGU

The appearance of more ice-phase particles in upper level, increasing ice crystals number and effective radius of graupel, together led to greater charge densities and as a consequence to stronger electric field intensities. Lightning will only be triggered if the electric field intensity is greater than a certain threshold, which means that aerosol tends to further affect lightning activity through electrification. Mansell et al. (2013) found that greater CCN concentration led to increased lightning activity up to a point, by affecting microphysical and electrical characteristics, with a large sensitivity to ice multiplication. In agreement with Mansell et al. (2013), this study showed that higher CCN concentration in the polluted case result in a relatively strong upper negative charge region, together with increased charge density and electric field intensity, finally enhancing lightning activity, as shown in Fig. 3b.

4.4 Convective strength

It is found that vertical convection strength did not varied significantly under different aerosol conditions (Fig. 7c and 8c). Previous studies showed that greater updraft was driven by increased microphysical latent heating, invigorating convection (Wang et al., 2011; Mansell and Ziegler, 2013; Altaratz et al., 2017). Figure 10 shows the vertical distribution of latent heat release at the developing and mature stage for both cases. It is evident that the vertical profiles of latent heating at 2-10 km are similar for different conditions. Considering that both cases have rather high CCN concentration, there would not be much difference between them in condensation.

The peak value of latent heating at higher level (11-14 km) is greater in the polluted case at this stage, with more ice-phase particles appearing (Fig. 7). The maximum latent heating of P-case (greater than 0.025 K s^{-1}), which could be from extra droplet freezing, appears near 12 km, while the latent heating of C-case is only 0.015 K s^{-1} at the same height. Previous studies also found that elevated aerosol loading contributed to the increasing frozen latent heat (e.g., Khain et al., 2005; Lynn et al. 2007; Storer et al., 2010). The increasing release of the latent heat of freezing strengthens the convection and further enhances charging and eventually lightning activity, as discussed above.

Atmospheric
Chemistry
and Physics
Discussions

Open Access

EGU

However, higher CCN concentration has little influence on condensation at lower level at this stage.

4.5 Delay of first flash in polluted case

370   As described above, the first lightning discharge was delayed in the polluted situation. In the meanwhile, the total charge density of the P-case is also weaker. The vertical charge distribution for the continental and polluted cases at the early development stage are shown in Figure 11d and 12d. It is clear that charge density in the C-case is greater than the P-case. The maximum of positive charge density of the C-case is more than +1 nC m^{-3} at 9 km, while the peak of the P-case is less than +0.5

375 nC m^{-3}. Compared to the C-case, the area where the charge density > +0.1 nC m^{-3} or < -0.1 nC m^{-3} is much smaller in the P-case (Fig. 12d).

     The differences of the charge density are further explored by examining the non-inductive charging mechanism. The polarity and magnitude of non-inductive charging depend on graupel-ice collision, and are related to environmental temperature and LWC,

380 which mainly occurs between -10 ℃ and -40 ℃ with sufficient LWC (Takahashi, 1978; Saunders et al., 1991; Saunders and Peck, 1998; Yair et al., 2010). In the present simulation, positive non-inductive charging rate exceeding 50 pC m^{-3} s^{-1} appears between 8 and 10 km in the C-case (Fig. 11b), corresponding to the positive charge region. Fig. 11a and 11c display the charge carried by different hydrometeors, which

385 indicate graupel charged positively in this region, mainly due to collisions of graupel and ice particles with relatively low temperature (-30 ℃). Compared to the C-case, the non-inductive charging rate is much lower (< 0.5 pC m^{-3} s^{-1}) in the P-case (Fig. 12b), resulting from lower graupel and ice particle concentrations and corresponding lower collision rates (Fig. 12a and 12c) at the beginning. With the further development of the

390 thunderstorm and the appearance of more ice-phase particles, the area where the charge density > +0.1 nC m^{-3} (or < -0.1 nC m^{-3}) becomes much larger at 09:30 UTC in the P-case (Fig. 13d), when it is more similar to the C-case at 09:18 UTC (Fig. 11d). In the meanwhile, the non-inductive charging rate increases significantly, resulting from the

appearance of more graupel particles (Fig. 13b).

395   High CCN concentration forces high concentrations of smaller droplets (Fig. 6a), making coalescence less efficient and delaying precipitation (Mansell and Ziegler, 2013). In the C-case, the earlier appearance of graupel probably led to earlier charging and thus lightning discharges

5 Conclusions and discussion

To elucidate the effects of aerosol on lightning activity, a two-moment bulk microphysics scheme (Mansell et al., 2010; Mansell and Ziegler, 2013) and bulk lightning model (BLM, Fierro et al., 2013) were coupled in the WRF model to simulate a multicell thunderstorm that occurred on 11 August 2017 in the metropolitan Beijing

405   area. The simulated distributions and spatio-temporal development of radar reflectivity are in overall agreement with observations.

Sensitivity experiments show that the intensity and duration of lightning activity are evidently different between moderate (continental) and high (polluted) aerosol concentrations, resulting from microphysical processes. Elevated aerosol loading

410   enhances the development of ice-phase microphysical processes, evidenced by more ice crystals and larger effective radius of graupel participating in charge-separation and electrification processes. As a result, non-inductive charging increases due to more frequent and effective collisions between graupel and other ice-phase particles. These lead to higher charge density, together with larger upper negative charge region which

415   is caused by more ice-phase particles transported to higher levels, leading to electric fields that surpass the threshold breakdown value, culminating in an enhanced lightning activity. During the developing and mature stages of the thunderstorm, the latent heat release at higher altitude is noticeably greater in the P-case, mainly due to the release of latent heat during freezing of supercooled liquid particles. But higher CCN

420   concentration has little influence on condensation at lower level at later stage compared to the continental CCN concentration, which already limits the development of excess supersaturation.

Compared to the C-case, initial lightning activity was delayed at the beginning of polluted thunderstorm in the P-case. A delay of the first flash was also found by Tan et

425 al. (2017), however, the advanced growth of graupel and ice crystals at the initiative time with lower CCN was not noted. In this study, raindrops and graupel appear earlier under continental condition at the beginning due to relatively efficient coalescence, helping to make downdrafts and lead to earlier non-inductive charging and lightning.

Observation and simulation studies found that elevated aerosol loading enhanced

430 the electrical activity (e.g., Koren et al., 2010; Wang et al., 2011). Some previous studies suggested that the mass mixing ratio of ice and graupel increased with the enhanced CCN concentration, eventually resulting in stronger lightning activity (e.g., Wang et al., 2011; Zhao et al., 2015), while a decrease of graupel mixing ratio was found by Tan et al. (2017). It should be noted that when aerosol concentrations are too

435 large, this leads to the inhibition of convection resulting in less lightning, as discovered by Altaratz et al. (2010) in the Amazon basin, as well as by Hu et al. (2019) in Houston region, and simulated by Mansell and Ziegler (2013). In this study, the enhancement of lightning activity under polluted condition results from increasing ice crystal number and effective radius of graupel particles. More ice-phase particles in upper level under

440 polluted condition, forming a relatively stronger negative charge region above the main positive charge center, which is also indicated by Zhao et al. (2015). We found that under continental condition, earlier charging results from advanced occurrence of graupel and ice crystals, providing support for the result of first discharge delay in the polluted thunderclouds (Tan et al., 2017).

445 The impacts of aerosol on lightning were investigated acting as CCN, however, aerosol also tends to affect electrification and lightning discharge by acting as ice nuclei (IN) through microphysical processes (Tao et al., 2012; Fan et al., 2017). More sensitive experiments are still needed to discuss the influences of aerosol on lightning due to microphysical and thermodynamic processes, acting as IN.

450

Data availability

To request the data given in this study, please contact Dr. Dongxia Liu at the Institute of Atmospheric Physics, Chinese Academy of Sciences, via email (liudx@mail.iap.ac.cn).

455

Author contributions

MS, XQ designed the research ideas for this study. MS carried the study out and prepared the paper. EM provided analysis ideas for the microphysics and electrification. DL and YY edited the paper. Other co-authors participated in science discussions and
460 article modification.

Competing interests

The authors declare that they have no conflict of interest.

Reference

470 Altaratz O, Kucienska B, Kostinski A B, et al. Global association of aerosol with flash density of intense lightning[J]. Environmental Research Letters, 2017, 12(11).

Altaratz O, Koren I, Yair Y, et al. Lightning response to smoke from Amazonian fires[J]. Geophysical Research Letters, 2010, 37(7).

Brooks I M, Saunders C P R, Mitzeva R P, et al. The effect on thunderstorm charging
475 of the rate of rime accretion by graupel[J]. Atmospheric Research, 1997, 43(3): 277-295.

Chaudhuri S, Middey A. Effect of meteorological parameters and environmental pollution on thunderstorm and lightning activity over an urban metropolis of India[J]. Urban Climate, 2013, 3: 67-75.

480 Dye J E, Knight C A, Toutenhoofd V, et al. The Mechanism of Precipitation Formation in Northeastern Colorado Cumulus III. Coordinated Microphysical and Radar Observations and Summary[J]. Journal of the Atmospheric Sciences, 1974, 31(8): 2152-2159.

Fan J, Zhang R, Li G, et al. Effects of aerosols and relative humidity on cumulus
485 clouds[J]. Journal of Geophysical Research: Atmospheres, 2007, 112(D14).

Fan J, Leung L R, Rosenfeld D, et al. Effects of cloud condensation nuclei and ice nucleating particles on precipitation processes and supercooled liquid in mixed-phase orographic clouds[J]. Atmospheric Chemistry and Physics, 2017, 17(2).

Fierro A O, Mansell E R, Mac Gorman D R, et al. The implementation of an explicit
490 charging and discharge lightning scheme within the WRF-ARW model: Benchmark simulations of a continental squall line, a tropical cyclone, and a winter storm[J]. Monthly Weather Review, 2013, 141(7): 2390-2415.

Guo J, Deng M, Lee S S, et al. Delaying precipitation and lightning by air pollution over the Pearl River Delta. Part I: Observational analyses[J]. Journal of
495 Geophysical Research: Atmospheres, 2016, 121(11): 6472-6488.

Hobbs P V, Rangno A L. Ice Particle Concentrations in Clouds[J]. Journal of the Atmospheric Sciences, 1985, 42(23): 2523-2549.

Hu J, Rosenfeld D, Ryzhkov A, et al. Polarimetric radar convective cell tracking reveals large sensitivity of cloud precipitation and electrification properties to CCN[J].
500 Journal of Geophysical Research: Atmospheres, 2019, 124(22): 12194-12205.

Jayaratne E R, Saunders C P R, Hallett J. Laboratory studies of the charging of soft-hail during ice crystal interactions[J]. Quarterly Journal of the Royal Meteorological Society, 1983, 109(461): 609-630.

Jiang M, Feng J, Sun R, et al. Potential influences of neglecting aerosol effects on the
505 NCEP GFS precipitation forecast[J]. Atmospheric Chemistry and Physics, 2017, 17(22):13967-13982.

18

Kar S K, Liou Y A, Ha K J. Aerosol effects on the enhancement of cloud-to-ground lightning over major urban areas of South Korea[J]. Atmospheric Research, 2009, 92(1):0-87.

510   Khain A, Rosenfeld D, Pokrovsky A. Aerosol impact on the dynamics and microphysics of deep convective clouds[J]. Quarterly Journal of the Royal Meteorological Society: A journal of the atmospheric sciences, applied meteorology and physical oceanography, 2005, 131(611): 2639-2663.

Khain A, Cohen N, Lynn B, et al. Possible Aerosol Effects on Lightning Activity and

515   Structure of Hurricanes[J]. Journal of the Atmospheric Sciences, 2008, 65(12):3652-3677.

Lynn B, Khain A, Rosenfeld D, et al. Effects of aerosols on precipitation from orographic clouds[J]. Journal of Geophysical Research: Atmospheres, 2007, 112(D10).

520   MacGorman D R, Rust W D, Schuur T J, et al. TELEX the thunderstorm electrification and lightning experiment[J]. Bulletin of the American Meteorological Society, 2008, 89(7): 997-1014.

Mansell E R, Ziegler C L. Aerosol effects on simulated storm electrification and precipitation in a two-moment bulk microphysics model[J]. Journal of the

525   Atmospheric Sciences, 2013, 70(7): 2032-2050.

Mansell E R, Ziegler C L, Bruning E C. Simulated electrification of a small thunderstorm with two-moment bulk microphysics[J]. Journal of the Atmospheric Sciences, 2010, 67(1): 171-194.

Mansell E R, MacGorman D R, Ziegler C L, et al. Charge structure and lightning

530   sensitivity in a simulated multicell thunderstorm[J]. Journal of Geophysical Research: Atmospheres, 2005, 110(D12).

Mitzeva R, Latham J, Petrova S. A comparative modeling study of the early electrical development of maritime and continental thunderstorms[J]. Atmospheric research, 2006, 82(1-2): 26-36.

535   Naccarato K P, Pinto Jr O, Pinto I. Evidence of thermal and aerosol effects on the cloud-to-ground lightning density and polarity over large urban areas of Southeastern

Brazil[J]. Geophysical Research Letters, 2003, 30(13).

Orville R E, Huffines G, Nielsen‐Gammon J, et al. Enhancement of cloud-to-ground lightning over Houston, Texas[J]. Geophysical Research Letters, 2001, 28(13): 2597-2600.

Price C. Global surface temperatures and the atmospheric electrical circuit[J]. Geophysical Research Letters, 1993, 20(13): 1363-1366.

Price C, Rind D. A simple lightning parameterization for calculating global lightning distributions[J]. Journal of Geophysical Research Atmospheres, 1992, 97(D9):9919-9933.

Qie X, Yuan S, Chen Z, et al. Understanding the dynamical-microphysical-electrical processes associated with severe thunderstorms over the Beijing metropolitan region[J]. Science China Earth Sciences, 2020: 1-17.

Qie X, Yuan T, Xie Y, et al. Spatial and temporal distribution of lightning activities on the Tibetan Plateau[J]. Chinese Journal of Geophysics, 2004, 47(6): 1122-1127.

Reynolds S E, Brook M, Gourley M F. Thunderstorm charge separation[J]. Journal of Meteorology, 1957, 14(5): 426-436.

Rosenfeld D, Lohmann U, Raga G B, et al. 2008. Flood or drought: How do aerosols affect precipitation?[J]. Science, 321(5894): 1309-1313.

Rosenfeld D, Woodley W L. 2000. Deep convective clouds with sustained supercooled liquid water down to -37.5 ℃[J]. Nature, 405(6785): 440.

Saunders C P R, Peck S L. Laboratory studies of the influence of the rime accretion rate on charge transfer during crystal/graupel collisions[J]. Journal of Geophysical Research: Atmospheres, 1998, 103(D12): 13949-13956.

Saunders C P R, Keith W D, Mitzeva R P. The effect of liquid water on thunderstorm charging[J]. Journal of Geophysical Research: Atmospheres, 1991, 96(D6): 11007-11017.

Srivastava A, Tian Y, Qie X S, et al. 2017. Performance assessment of Beijing Lightning Network (BLNET) and comparison with other lightning location networks across Beijing. Atmospheric Research, 197 76-83.

Stolz D C, Rutledge S A, Pierce J R. Simultaneous influences of thermodynamics and

Atmospheric
Chemistry
and Physics
Discussions

aerosols on deep convection and lightning in the tropics[J]. Journal of Geophysical Research: Atmospheres, 2015, 120(12): 6207-6231.

570   Storer R L, Van Den Heever S C, Stephens G L. Modeling aerosol impacts on convective storms in different environments[J]. Journal of the Atmospheric Sciences, 2010, 67(12): 3904-3915.

Sun M, Qie X, Liu D, et al. Analysis of potential effects of aerosol on lightning activity in Beijing metropolitan region[J]. Chinese Journal of Geophysics, 2020, 63(5): 1766-1774.

575   Takahashi T. A numerical simulation of winter cumulus electrification. Part I: Shallow cloud[J]. Journal of the Atmospheric Sciences, 1983, 40(5): 1257-1280.

Takahashi T. Riming electrification as a charge generation mechanism in thunderstorms[J]. Journal of the Atmospheric Sciences, 1978, 35(8): 1536-1548.

Tan Y B, Ma X, Xiang C Y, et al. A numerical study of the effects of aerosol on
580   electrification and lightning discharges during thunderstorms[J]. Chinese Journal of Geophysics, 2017, 60(8): 3041-3050.

Tao W K, Chen J P, Li Z, et al. Impact of aerosols on convective clouds and precipitation[J]. Reviews of Geophysics, 2012, 50(2).

Thomas R J, Krehbiel P R, Rison W, et al. Observations of VHF source powers radiated
585   by lightning[J]. Geophysical Research Letters, 2001, 28(1): 143-146.

Thornton J A, Virts K S, Holzworth R H, et al. 2017. Lightning enhancement over major oceanic shipping lanes[J]. Geophysical Research Letters, 44(17).

Twomey, S., 1959: The nuclei of natural cloud formation, Part II: The supersaturation in natural clouds and the variation of cloud droplet concentration. Geofis. Pura
590   Appl., 43, 243–249.

Wang Q, Li Z, Guo J, et al. 2018. The climate impact of aerosols on the lightning flash rate: is it detectable from long-term measurements?[J]. Atmospheric Chemistry and Physics, 18(17).

Wang Y, Qie X S, Wang D F, et al. 2016. Beijing Lightning Network (BLNET) and the
595   observation on preliminary breakdown processes [J]. Atmos. Res., 171: 121–132.

Wang Y, Wan Q, Meng W, et al. Long-term impacts of aerosols on precipitation and

lightning over the Pearl River Delta megacity area in China[J]. Atmospheric Chemistry and Physics, 2011, 11(23): 12421-12436.

Westcott N E. Summertime cloud-to-ground lightning activity around major Midwestern urban areas[J]. Journal of Applied Meteorology, 1995, 34(7): 1633-1642.

Williams E, Mushtak V, Rosenfeld D, et al. Thermodynamic conditions favorable to superlative thunderstorm updraft, mixed phase microphysics and lightning flash rate[J]. Atmospheric Research, 2005, 76(1-4): 288-306.

Williams E, Stanfill S. The physical origin of the land–ocean contrast in lightning activity[J]. Comptes Rendus Physique, 2002, 3(10): 1277-1292.

Williams E. The tripole structure of thunderstorms[J]. Journal of Geophysical Research, 1989: 13151-13167.

Xiong Y J, Qie X S, Zhou Y J, et al. Regional responses of lightning activities to relative humidity of the surface[J]. Chinese Journal of Geophysics, 2006, 49(2): 311-318.

Yair Y. Lightning hazards to human societies in a changing climate[J]. Environmental Research Letters, 2018, 13(12).

Yair Y, Lynn B, Price C, et al. Predicting the potential for lightning activity in Mediterranean storms based on the Weather Research and Forecasting (WRF) model dynamic and microphysical fields[J]. Journal of Geophysical Research, 2010.

Yair Y. Charge generation and separation processes[J]. Space Science Reviews, 2008, 137(1-4): 119-131.

Yuan T, Remer L A, Pickering K E, et al. Observational evidence of aerosol enhancement of lightning activity and convective invigoration[J]. Geophysical Research Letters, 2011, 38(4).

Zhao P, Li Z, Xiao H, et al. Distinct aerosol effects on cloud-to-ground lightning in the plateau and basin regions of Sichuan, Southwest China[J]. Atmospheric Chemistry and Physics, 2020, 20(21): 13379-13397.

Zhao P, Yin Y, Xiao H. The effects of aerosol on development of thunderstorm electrification: A numerical study[J]. Atmospheric Research, 2015, 153: 376-391.

22

Ziegler C L. Retrieval of thermal and microphysical variables in observed convective

storms. Part 1: Model development and preliminary testing[J]. Journal of the

Atmospheric Sciences, 1985, 42(14): 1487-1509.

630

Table1. Settings for the nested simulations

Model Option	Outer D01	Inner D02
Domain Coverage	6km, 442×391	2km, 496×496
Vertical levels	40	40
Time step	30s	10s
Microphysics Scheme	NSSL	NSSL
Longwave Radiation	RRTM	RRTM
Shortwave Radiation	Dudhia	Dudhia
Boundary Layer	BouLac PBL	BouLac PBL
Land Surface	Unified Noah LSM	Unified Noah LSM

635
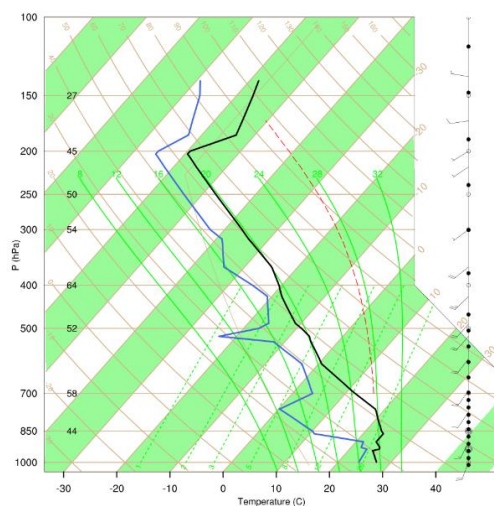
Figure 1 Sounding profiles for Beijing at 12:00 UTC on Aug11, 2017. The black, blue solid lines and red dashed line represent temperature, dew point, parcel adiabatic lapse rate, respectively.

640
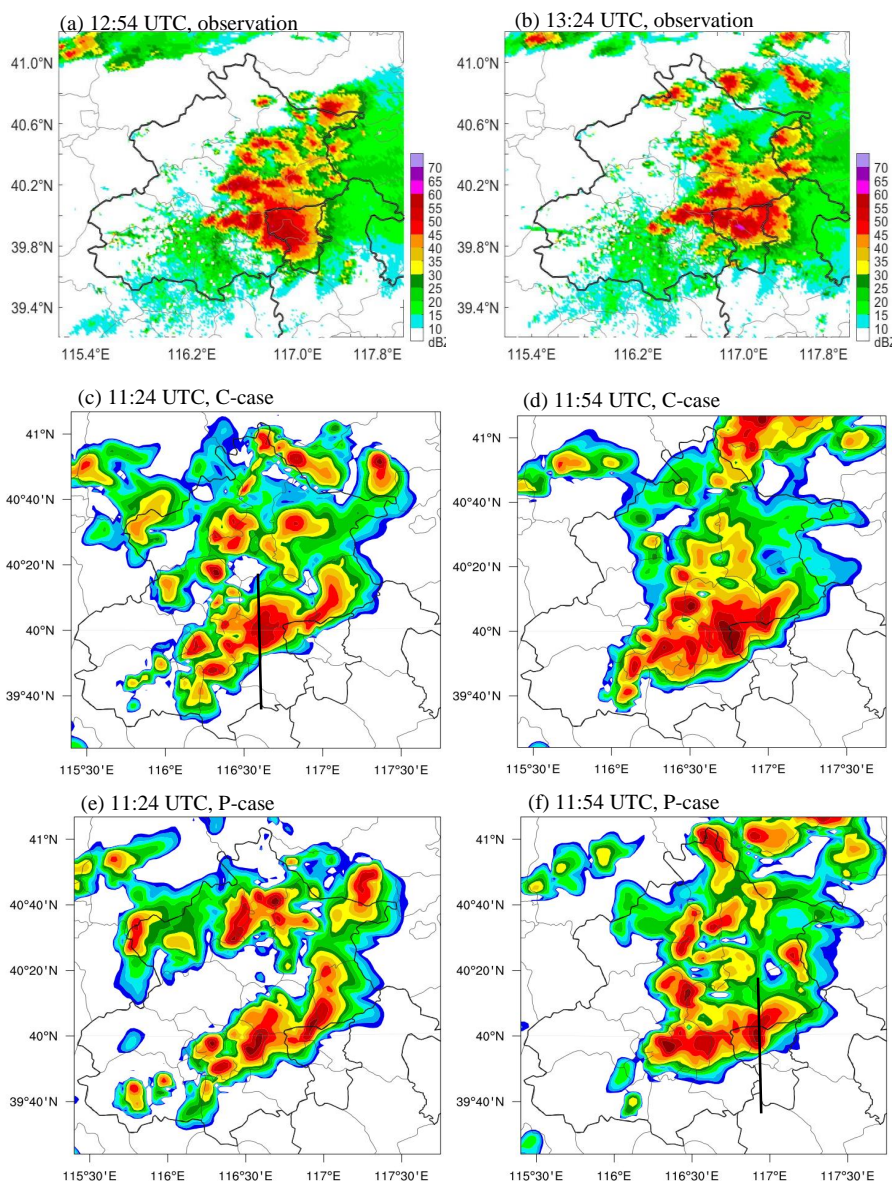
Figure 2 Radar reflectivity (unit: dBZ) between observation and simulation for the C- and P-cases, the simulation was earlier than observation about 1.5 h. (a)-(b) Observation at 12:54 UTC and 13:24 UTC. (c)-(d) Simulation for the C-case at 11:24 UTC and 11:54 UTC. (e)-(f) Simulation for the P-case at 11:24 UTC and 11:54 UTC, respectively.

650
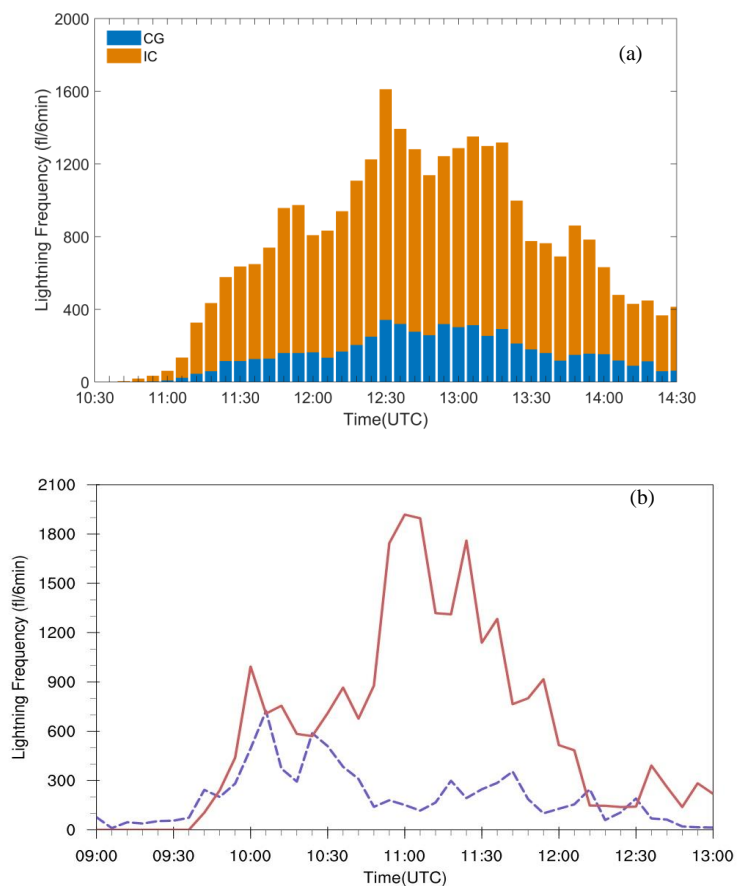
Figure 3 Temporal variation in (a) observed total lightning frequency and (b) simulated lightning

frequency. In (a), orange represents IC lightning and blue represents CG lightning. In (b), solid line

655   represents the P-case and dashed line represents the C-case.
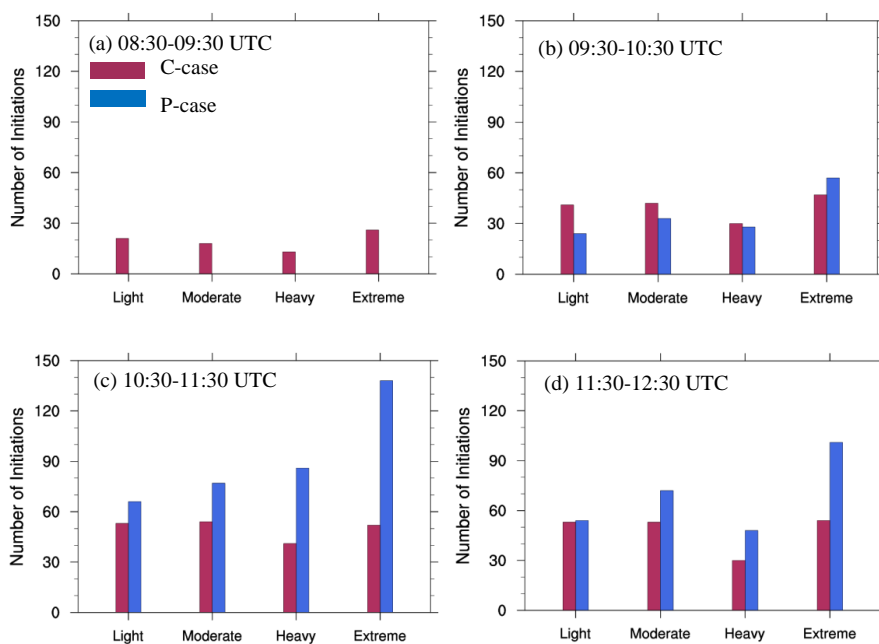
660   **Figure 4** Number of initiations for different lightning categories in different time, i.e. light (50-100 grids), moderate (100-200 grids), heavy (200-300 grids) and extreme (>300 grids), simulated for the P- and C-cases.

665
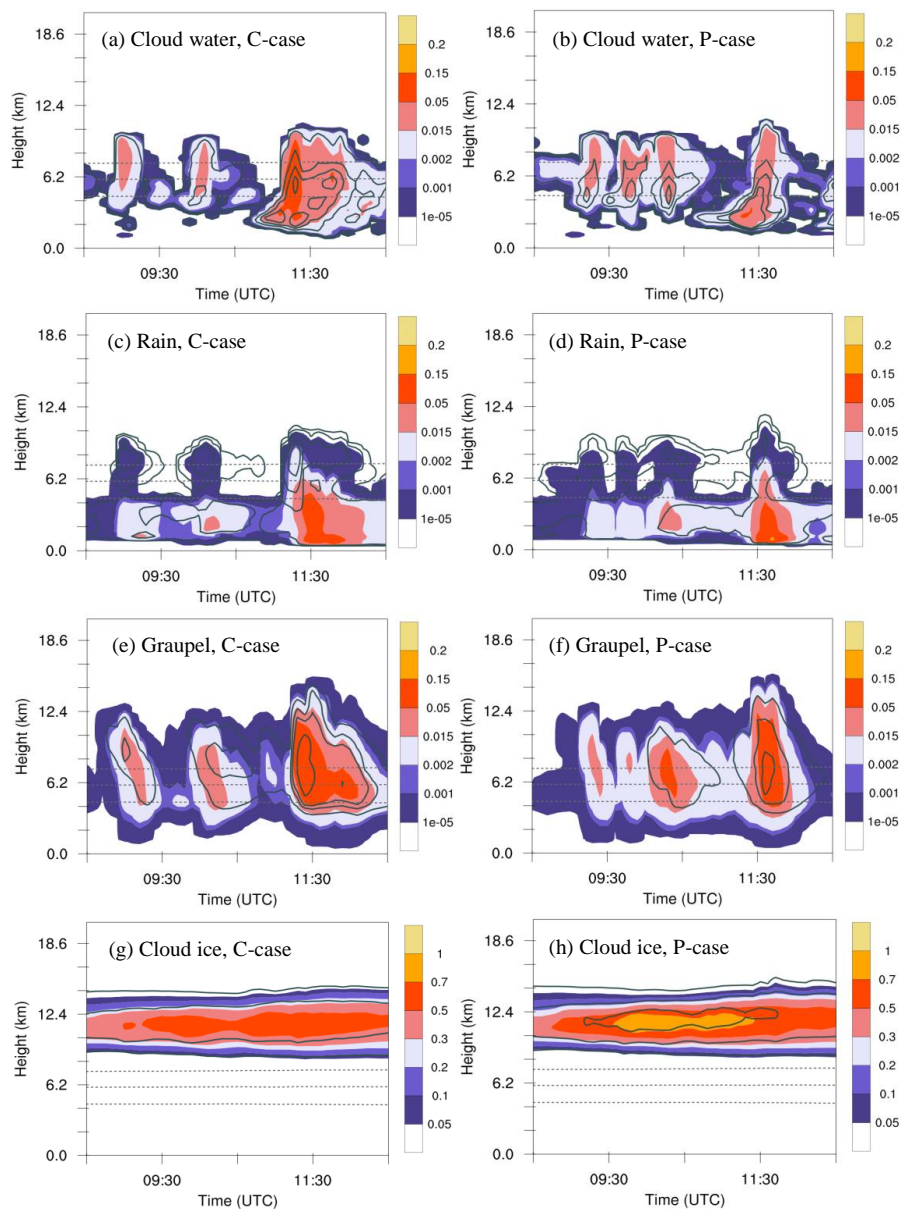
670   (figure continued on next page)
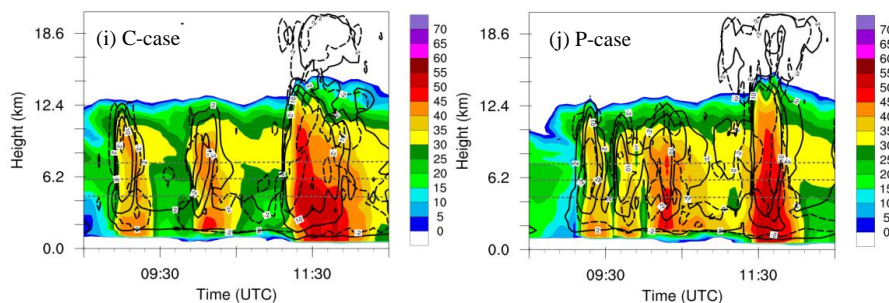
Figure 5 (a)-(h) Temporal variation of the vertical profiles of domain-averaged mass mixing ratio (g kg⁻¹, shaded) and number concentration (kg⁻¹, solid lines) of (a) cloud water in the C-case, (b) cloud water in P-case, (c) rain water in the C-case, (d) rain water in the P-case, (e) graupel in the C-case, (f) graupel in the P-case, (g) ice in the C-case, and (h) ice in the P-case. The 0 °C, -10 °C, and -20 °C isotherms are shown by the dashed gray lines in (a)-(h). Contour levels in (a)-(h) for cloud water number concentration are 10^5, 10^6, 10^7, 2×10^7, 3×10^7 kg⁻¹, and for rain water are 1, 10, 10^2, 10^3, 3×10^3 kg⁻¹, and for graupel are 10, 30, 50, 100, 300, 500, 700, 1000 kg⁻¹, and for ice are 0.1×10^7, 1×10^7, 3×10^7 kg⁻¹. (i)-(j) Time-height maximum simulated radar reflectivity (color shading, unit: dBZ) and vertical velocities (solid line: 2, 10 m s⁻¹; dashed line: -2 m s⁻¹) for (i) the C-case and (j) the P-case.
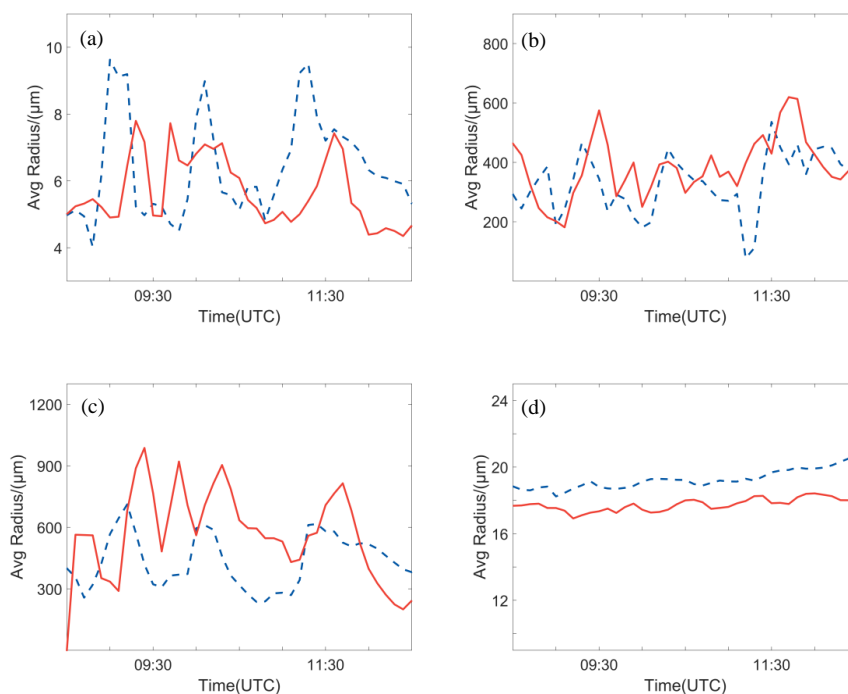
685

Figure 6 Temporal variation of domain-averaged effective radius for the different hydrometeors. (a) cloud water, (b) rainwater, (c) graupel, (d) ice. The solid lines represent the P-case and the dashed lines represent the C-case.

690
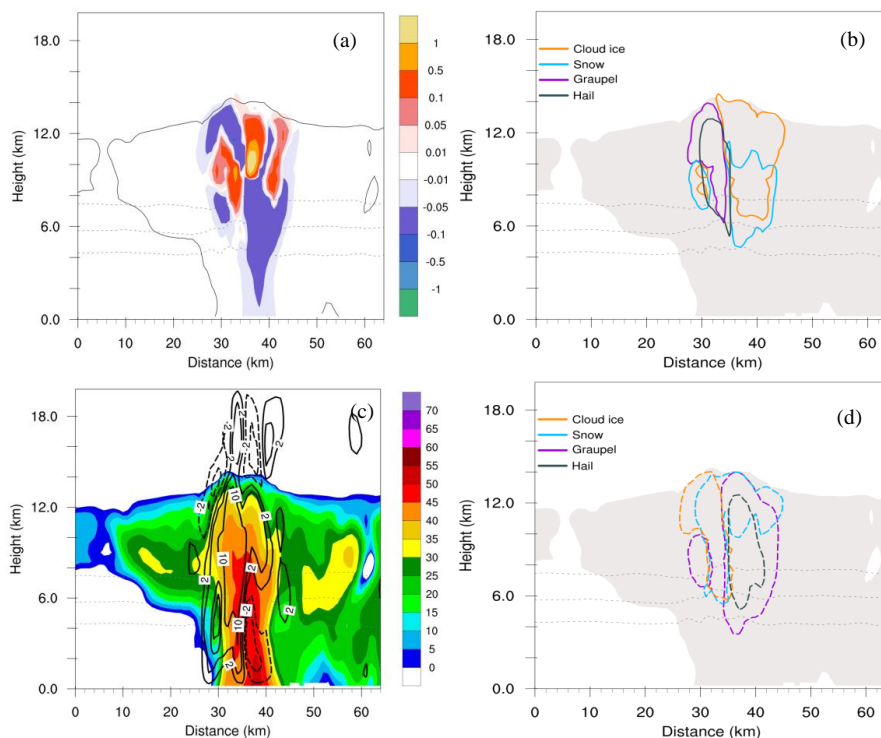
Figure 7 Vertical cross sections (south to north) at the location shown in Fig. 2f of the main electrical
and microphysical variables at the mature stage of the thunderstorm (11:54 UTC) in the P-case. (a)

695 Total net space charge (nC m^{-3}, shaded). The 0 ℃, -10 ℃, and -20 ℃ isotherms are shown by
dashed gray lines in (a)-(d). (b) +0.1 nC m^{-3} space charge density contours for cloud ice (orange),
snow (blue), graupel (purple), and hail (black). The cloud outline (reflectivity echoes ≥5 dBZ) is
denoted by the gray shaded contour. (c) Radar reflectivity (unit: dBZ), black lines for vertical
velocities (solid line: 2, 5, 10 m s^{-1}; dashed line: -2 m s^{-1}). (d) As in (b), but for -0.1 nC m^{-3} charge

700 density.

Figure 8 As in Fig. 7, but the vertical cross sections at the location shown in Fig. 2c of the main
electrical and microphysical variables at the mature stage of the thunderstorm (11:24 UTC) in the
C-case.
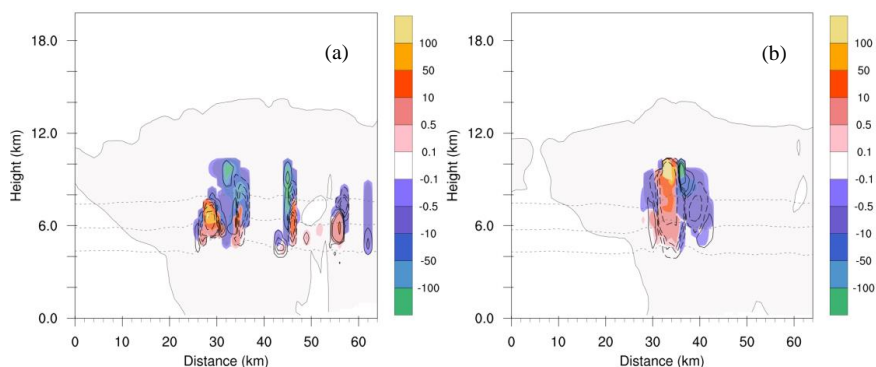
Figure 9 Vertical cross sections (south to north) at the location shown in Fig. 2 of non-inductive (pC m^{-3} s^{-1}, shaded) and inductive (solid lines: 0.1, 0.5, 1 pC m^{-3} s^{-1}; dashed lines: -0.1, -0.5, -1, -5, -10 pC m^{-3} s^{-1}) charging rates at the mature stage of (a) C-case (11:24 UTC, Fig. 2c), and (b) P-case (11:54 UTC, Fig. 2f). The 0 °C, -10 °C, and -20 °C isotherms are shown by dashed gray lines.
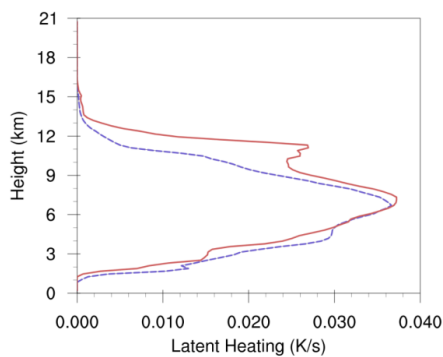
Figure 10 Vertical profiles of domain-maximum latent heating (unit: K s^{-1}), at the developing and mature stage (09:30-12:00 UTC). The solid line represents the P-case and the dashed line represents the C-case.
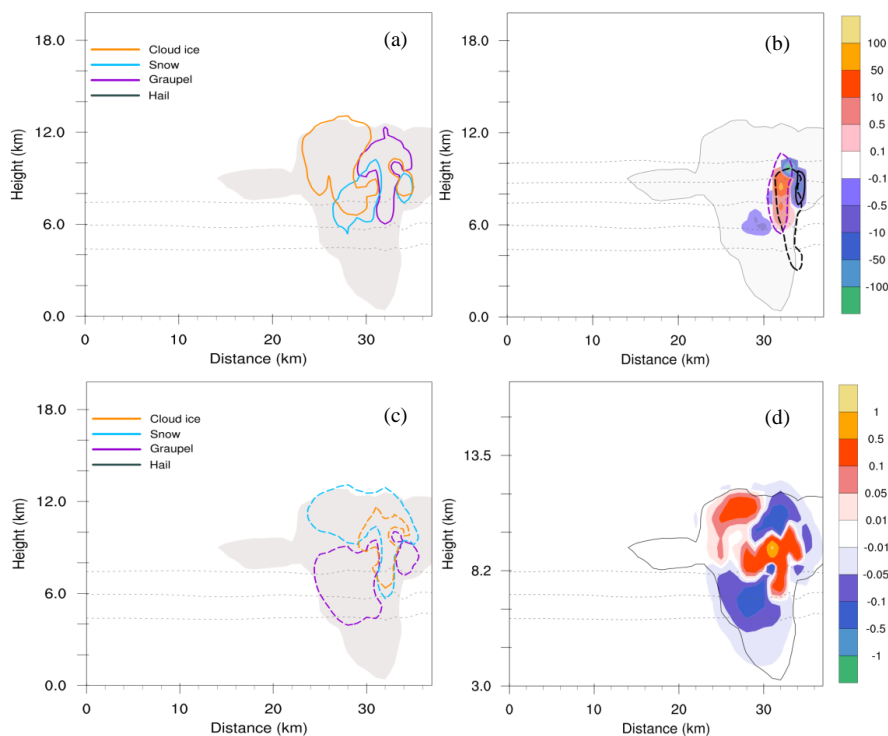
Figure 11 Vertical cross sections (south to north) of main electrical and microphysical variables at the beginning of the thunderstorm (09:18 UTC) in the C-case. (a) +0.1 nC m^{-3} space charge density contours for cloud ice (orange), snow (blue), graupel (purple), and hail (black). The cloud outline (reflectivity echoes ≥5 dBZ) is denoted by the gray shaded contour. (b) Non-inductive (shaded) and inductive (solid black line) charging rate (unit: pC m^{-3} s^{-1}), dashed black line for LWC (1 g kg^{-1}), dashed violet line for graupel (0.5, 3 g kg^{-1}). (c) As in (a), but for -0.1 nC m^{-3} charge density. (d) Total net space charge (nC m^{-3}, shaded). The 0 °C, -10 °C, and -20 °C isotherms are shown by dashed gray lines in (a)-(d).
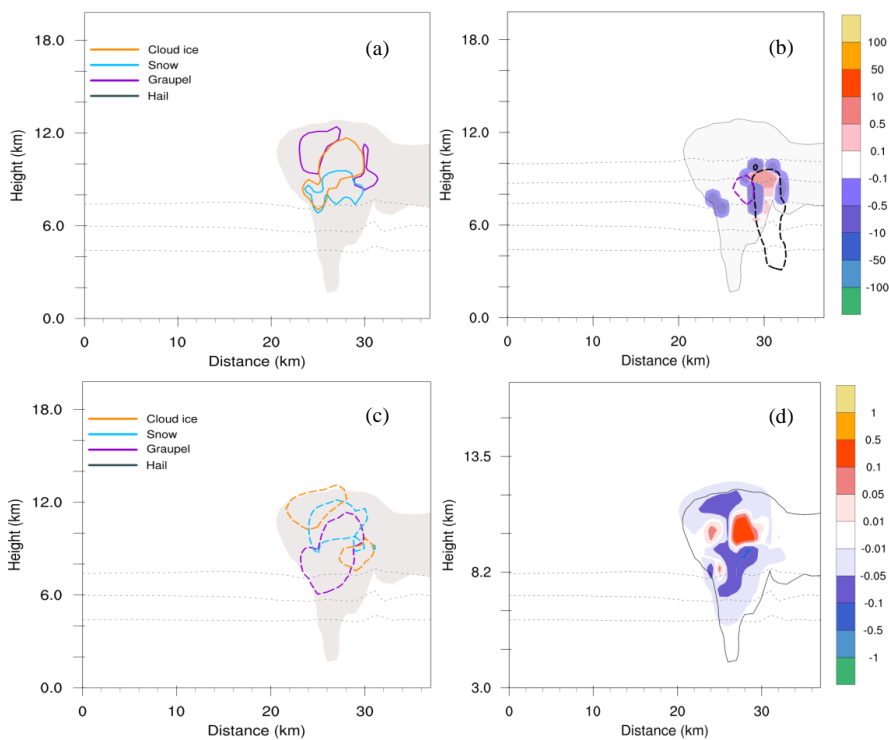
735

Figure 12 As in Fig. 11, but the vertical cross sections at the beginning of the thunderstorm (09:18 UTC) in the P-case.

740
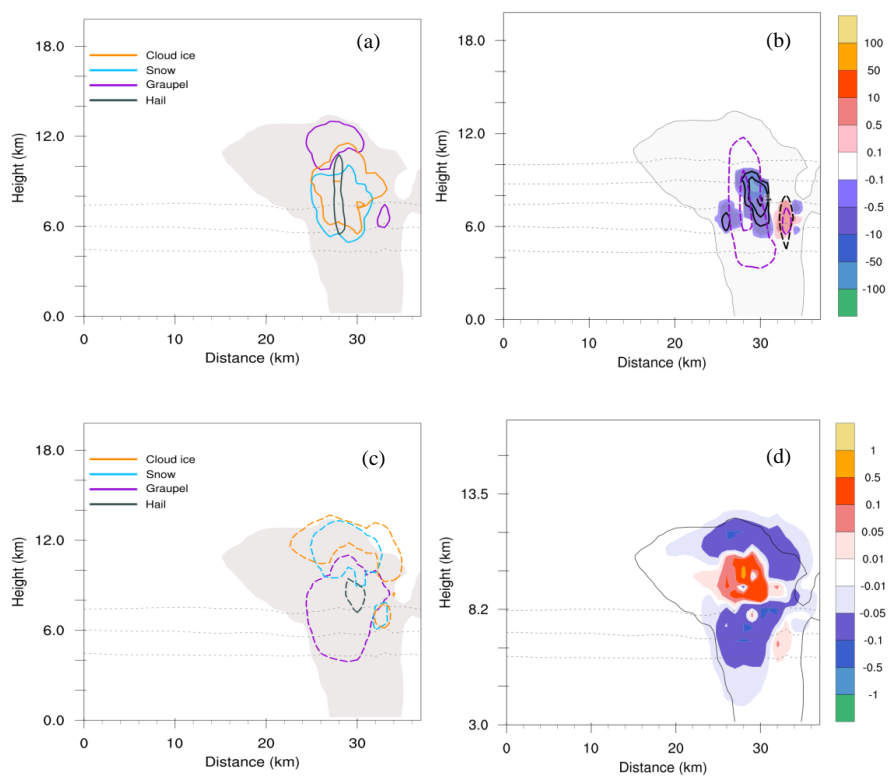
Figure 13 As in Fig. 11, but the vertical cross sections later than the beginning of the thunderstorm (09:30 UTC) in the P-case.